Hydrodynamic model for *Spiroplasma* motility

Christian Esparza López and Eric Lauga*
Department of Applied Mathematics and Theoretical Physics, University of Cambridge, Cambridge CB3 0WA, United Kingdom

(Received 4 April 2020; accepted 31 July 2020; published 8 September 2020)

Spiroplasma is a small helical bacterium that swims and performs chemotaxis in a non-conventional way. Equipped with a flexible flat ribbon cytoskeleton, *Spiroplasma* deforms its body into a helix that periodically changes its chirality. The helical transformation produces a kink that propagates along the cell body and propels the microorganism in the opposite direction. Based on experimental observations, we develop a hydrodynamic model to describe *Spiroplasma* motility. We obtain expressions for the total linear and angular displacements of the cell body per swimming stroke. We show mathematically that the cell body does not reorient at the end of one period, which allows us to define an effective swimming speed, v_s. We then use v_s to calculate the energy dissipated in one stroke, $\dot{W}$, and to define a hydrodynamic efficiency, $\eta = \dot{W}_0/\dot{W}$, where $\dot{W}_0$ is the power spent by a straight filament moving at the same speed v_s. We show that the helical shape of the cytoskeleton that maximizes both v_s and η are helices of pitch angles ϕ close to that of *Spiroplasma*, $\phi \simeq 35^\circ$, in agreement with experimental observations and with previous numerical simulations.

DOI: 10.1103/PhysRevFluids.5.093102

I. INTRODUCTION

The world of swimming microorganisms, often found in liquid environments, may appear strange to our everyday experience. This is the realm of low-Reynolds-number flow, where inertia is negligible and viscous forces dominate. The strategies to achieve locomotion in such an environment are different from those we know for macroscopic swimming creatures. In particular, a small organism such as a bacterium must move in a nonreciprocal fashion (i.e., its motion is different when observed forward in time compared to backward in time) in order to achieve net locomotion [1].

A natural way to achieve this type of deformation is by propagating waves [2]. Indeed, most swimming microorganisms have evolved to grow slender appendages called flagella, which can be deformed into flexible waves or rotated in apparent waves [3–5]. Many species of bacteria, such as *Escherichia coli* (*E. coli*), use helical flagellar filaments and rotate them along their axes. As a result, the helical filaments push on the surrounding fluid and generate propulsion in the opposite direction [6]. There exist, however, some bacteria that do not rely on flagella to achieve locomotion. This is the case of the marine bacterium *Synechococcus*, whose swimming strategy is still under debate [7,8], and the better-known *Spiroplasma*, which swims by deforming its helical body [9,10] (see illustration in Fig. 1).

As opposed to the *Spirochetes*, which have internal flagella [11], *Spiroplasma* is a wall-less bacterium (termed a mollicute) with an internal, flexible flat ribbon cytoskeleton. The cell deforms its cytoskeleton into a helix whose chirality is allowed to progressively shift [12–19]. The change

*e.lauga@damtp.cam.ac.uk

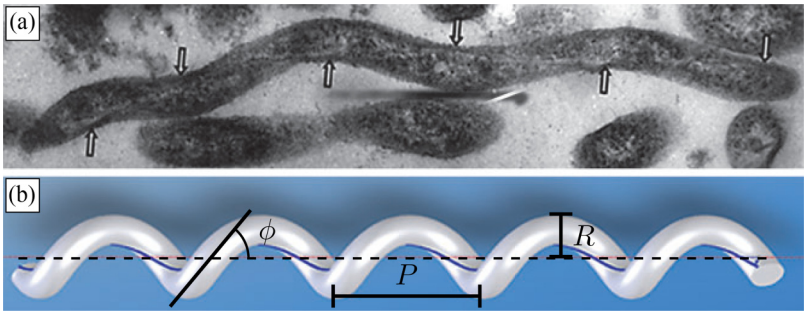

FIG. 1. The bacterium *Spiroplasma* with its characteristic helical shape. (a) Electron micrograph of *Spiroplasma*, with the arrows showing the cytoskeleton along the shortest helical path. (b) A three-dimensional model of an average cell with helical radius R and pitch $P = 2\pi R \cot\phi$, where ϕ is the pitch angle. (Reprinted from Ref. [16] and modified from Ref. [12]. With permission from S. Karger AG and John Wiley and Sons.)

in geometry gives rise to a wall domain, i.e., a kink, which propagates along the cell body from one end to the other. The chirality is then reverted in a similar fashion completing a swimming stroke [10,20–22]. The whole deformation is nonreciprocal, therefore movement at a low Reynolds number is possible, and indeed, the bacterium is observed to move in the direction opposite to the kink pair propagation.

The cell body has a definite polarity, as one of its ends is tapered, usually called the tip (or head), while the other untapered end is termed the tail. It has been observed that kinks appear most of the times at the tip [18]. As a consequence, *Spiroplasma* swims predominantly in the direction of the head. The morphological change is stochastic in nature and the motion of the kinks is altered by the presence of different amino acids [18,23,24]. Analogously to the well-studied *E. coli* chemotaxis [6], modulation of the rate of chirality transformations allows *Spiroplasma* to follow chemical concentration gradients. However, studies have yet to discover the genes involved [18], and therefore the precise mechanism that controls chemotaxis remains unclear.

Hydrodynamic models used to describe the locomotion of *Spiroplasma* motility have been previously developed [20–22]. These studies show three main results: (i) the cell moves in the direction opposite to the kink pair propagation, with a speed proportional to the kink speed; (ii) the helical pitch of *Spiroplasma* (angle $\phi \simeq 35^\circ$) maximizes the hydrodynamic swimming efficiency; and (iii) at the optimum pitch angle, the interkink distance that maximizes the swimming speed is $D/L \approx 1/3$ [20–22], where L is the total axial length of the helical cell. These results are obtained mostly numerically and were supported by theoretical predictions using some fitting parameters.

In this study, we propose a coarse-grained mathematical model that avoids the use of fitting parameters. In the spirit of previous studies, we model *Spiroplasma* as a deformable body whose motion in fluids can be described by the resistive-force theory of slender filaments [25]. We derive analytical expressions for the swimming speed and the swimming efficiency, which we then optimize.

This paper is organized as follows. In Sec. II we develop the mathematical model. We first present the geometry of *Spiroplasma* and the kinematics and dynamics of the motion. We then describe the swimming gait in detail and compute the resistance matrix for the slender body using resistive-force theory. At the end of Sec. II we introduce our coarse-grained model allowing us to take into account the helical geometry of *Spiroplasma*.

The theoretical results derived from our model are then presented in Secs. III and IV. First, we consider the nonhelical case in Sec. III, where we replace the cell body with a straight rod located at the position of the original helical axis. The rod is allowed to bend similarly to *Spiroplasma*, producing a kink that propagates from end to end and propels the rod (i.e., the cell) in the opposite direction. In this case, we demonstrate that the average orientation of the cell body is unchanged by

the swimming stroke, which allows us to define an effective swimming speed and a hydrodynamic efficiency. We next show in Sec. IV that this conclusion is robust to the inclusion of the helical geometry at a coarse-grained level and therefore the cell undergoes no periodic reorientation.

The results of our models are presented in Sec. V and numerical solutions are compared to asymptotic results in the limit of a small-interkink distance. We compute, in particular, the optimum pitch angle and show that it is close to the experimental value of $\phi \approx 35^\circ$. We finally summarize our results and discuss their relevance to cell diffusion and chemotaxis in Sec. VI.

II. SETUP AND MODEL

A. Geometry and notation

The bacterium *Spiroplasma melliferum* has a right-handed helical body of radius $R \simeq 0.5\ \mu$m, pitch $P \simeq 1\ \mu$m, and four to six helical repeats [13] (see notation in Fig. 1). The cell body is therefore roughly 10 times longer than it is wide. As mentioned above, the cytoskeleton allows the cell to change its chirality from right-handed to left-handed. It has been observed that the change occurs in the absence of external stress, therefore the body displays a kink with angle $\theta = \pi - 2\phi \simeq 110^\circ$, where $\phi \simeq 35^\circ$ is the pitch angle of the helical body [10,22,26,27]. The angle θ is therefore the angle between the axes of the helical domains with opposite handedness. The time between chirality changes is observed to be exponentially distributed in experiments, at rate $\lambda_k = 1\ \text{s}^{-1}$, while the time between a kink pair follows a normal distribution with mean $\tau_p = 0.26$ s. The kink pair propagates along the helical filament at average speed $v_k \simeq 10.5 \pm 0.3\ \mu$m/s, which is linearly related to the swimming velocity $v_s \simeq 3.3 \pm 0.2\ \mu$m/s [10].

A chirality transformation under the stress-free constraint allows for two kind of kinematic modes, namely, the "crankshafting" and the "speedometer cable" modes [27]. In the former, one of the domains revolves around the other, while in the latter, both domains spin around their axes. Scaling arguments for the energy dissipated on each mode suggest that the speedometer cable transformations are predominant, as observed in experiments [10,22]. Given the aspect ratio of the cell body, we model the organism as a deformable rod that represents the location of the axes of the helical domains and that performs the speedometer swimming stroke illustrated in Fig. 2. The details of the helical geometry are included by allowing the drag on the rod to depend on the pitch angle of the original helical body and by including the hydrodynamic propulsive forces that originate from the rotation of the helical domains in the speedometer cable swimming mode. After one stroke, the position of the head $\mathbf{H}$ is denoted by $\mathbf{H}(T) = \mathbf{H}(0) + \mathbf{X}_T$, where $\mathbf{H}(0)$ is the initial position of the head and $\mathbf{X}_T$ the net displacement after one period. The orientation at the end of the stroke will be $\mathbf{n}(T) = \mathbf{R}_T \cdot \mathbf{n}(0)$, where $\mathbf{R}_T$ is a rotation matrix and $\mathbf{n}(0)$ a unit vector that defines the initial orientation of the cell body (assumed to be straight at the beginning of the stroke). The linear and angular displacements, $\mathbf{X}_T$ and $\varphi_T = \cos^{-1}(\mathbf{n}(T) \cdot \mathbf{n}(0))$, are obtained by computing the force and torque acting on the body.

B. Dynamics

Using the resistive-force theory for slender filaments subject to viscous flows [25], we decompose the hydrodynamic force acting on the model rod, in parallel and perpendicular components to the filament, as

$$\mathbf{f} = -\zeta_\perp[\beta\boldsymbol{\tau}\boldsymbol{\tau} + (\mathbf{1} - \boldsymbol{\tau}\boldsymbol{\tau})] \cdot \mathbf{v}, \tag{1}$$

where $\mathbf{f}$ is the hydrodynamic force per unit length, $\mathbf{v} = \mathbf{U} + \boldsymbol{\Omega} \times \mathbf{x} + \dot{\mathbf{x}}$ is the velocity of the fluid at a point $\mathbf{x}(s,t)$ along the centerline of the rod (i.e., the axis of the helical domains) and where $\mathbf{U}$ and $\boldsymbol{\Omega}$ denote the linear and angular velocities of the body in the laboratory frame of reference. Here $\mathbf{x}(s,t)$ is a suitable parametrization of the cell body in terms of the arclength s, in a frame of reference comoving with some arbitrary point of the cell body at time t. In the following section we

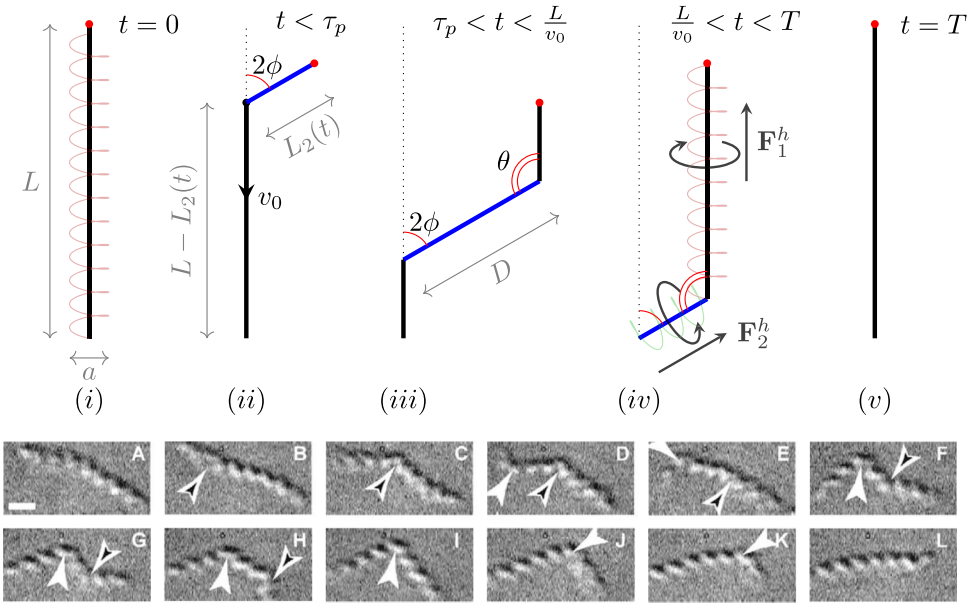

FIG. 2. Illustration of the swimming stroke of *Spiroplasma*. (i)–(v) Our mathematical model where we consider the helical axis of the swimmer as being made of one, two, or three straight rods (thick lines). The stroke is described in the frame of reference in which the tail (the untapered end) is static. (A, i) Initially the cell body has a right-handed helical shape. (B, C, ii) A kink appears at $t = 0$ and propagates from head (red circle) to tail along the body of axial length L at speed $v_0 = v_k \cos\phi$. In that case, the deformed rod has two domains of size $L_2(t)$ and $L_1(t) = L - L_2(t)$. (D–H, iii) The second kink forms at $t = \tau_p$; the maximum distance between kinks is denoted by $D = v_0\tau_p$. The deformed rod now has three domains. (I–K, iv) The configuration is similar to that in (ii), with reversed signs of the forces and torques acting on the body; the blue segment now has left-handed chirality and rotates clockwise, while the right-handed segment rotates anticlockwise. The arrowhead shows the induced force. (L, v) The stroke finishes at $T = \tau_p + L/v_0$. [(A–L) Experiments reprinted from Ref. [10] with permission from Elsevier.]

divide the swimming stroke into different stages, and we specify the parametrization and the frame of reference used in each one of them.

We use primes to denote spatial derivatives along the arclength of the rod and overdots for time derivatives, so the tangent vector at $\mathbf{x}$ is denoted by $\boldsymbol{\tau} \equiv \mathbf{x}'$ and $\dot{\mathbf{x}}$ is the velocity of deformation. In Eq. (1) the identity tensor is represented by $\mathbf{1}$, the drag coefficient per unit length, perpendicular to the body, is denoted by $\zeta_\perp$, and $\beta = \zeta_\parallel/\zeta_\perp$ is the ratio of the parallel to the perpendicular drag coefficients.

The total force $\mathbf{F}$ and torque $\mathbf{N}$ acting on the body at a given time are obtained by integrating Eq. (1) along the arclength of the model rod $\mathbf{x}(s,t)$, i.e.,

$$\mathbf{F}(t) = \int_{\mathbf{x}(s,t)} \mathbf{f}(s,t)\,\mathrm{d}s, \tag{2}$$

$$\mathbf{N}(t) = \int_{\mathbf{x}(s,t)} \mathbf{x}(s,t) \times \mathbf{f}(s,t)\,\mathrm{d}s. \tag{3}$$

Assuming free swimming, drag and thrust must balance, and therefore we have the constraints $\mathbf{F} = \mathbf{0}$ and $\mathbf{N} = \mathbf{0}$. Consequently, $\mathbf{U}$ and $\boldsymbol{\Omega}$ can be expressed in terms of integrals of $\dot{\mathbf{x}}$. Then $\mathbf{X}_T$, $\mathbf{R}_T$ can be

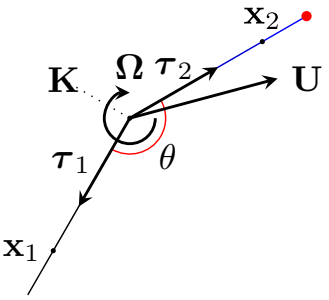

FIG. 3. First stage of the swimming stroke in the interval $0 \leqslant t \leqslant \tau_p$. We describe the motion in a frame of reference in which the tail appears to be fixed, with instantaneous origin at the location of the kink, $\mathbf{K}(t)$. The body moves with linear velocity $\mathbf{U}(t)$ and rotates with angular velocity $\boldsymbol{\Omega}(t)$. Material points on the axis of the right-handed and left-handed domains are denoted by $\mathbf{x}_1$ and $\mathbf{x}_2$, respectively. The unit tangent vectors along the domains are denoted by $\boldsymbol{\tau}_1$ and $\boldsymbol{\tau}_2$.

obtained by integration over one stroke as

$$\mathbf{X}_T = \int_0^T \dot{\mathbf{H}}(t)\,\mathrm{d}t, \tag{4}$$

$$(R_T)_{ij} = \mathcal{T} \exp\left[\epsilon_{ikj} \int_0^T \Omega_k(t)\,\mathrm{d}t\right], \tag{5}$$

where ϵ_{ijk} are the components of the Levi-Civita pseudotensor and $\dot{\mathbf{H}}(t)$ depends on $\mathbf{U}$ and $\boldsymbol{\Omega}$ in a nontrivial way. The operator $\mathcal{T}$ is called the time ordering operator, which ensures that the infinitesimal rotations $\epsilon_{ijk}\Omega_k(t)$, in the Taylor expansion of the exponential function, appear from left to right in decreasing order of time evaluation.

In the next section we describe in detail the model for the swimming stroke depicted in Fig. 2 and calculate the forces and torques acting on the body in each stage.

C. Swimming stroke

The motion of the cell starts at $t = 0$ when a kink appears [see arrowheads in Figs. 2(B) and 2(C)] and starts propagating from head (tapered end) to tail at speed $v_0 = v_k \cos(\phi) = v_k \sin(\theta/2)$, which is the projected speed on the axis of the helical body. This is the first stage, which ends at time τ_p when a second kink appears [Figs. 2(i), 2(ii), and 2(A)–2(C)]. During the second stage, the kink pair propagates along the body with a fixed distance $D = v_0\tau_p$ between the kinks [Figs. 2(iii) and 2(D)–2(H)]. The third stage starts when the first kink reaches the tail at time $t = L/v_0$, and during this stage the second kink continues propagating until it reaches the tail. At the end of the third stage the geometry of the cell reverts to its original straight configuration [Figs. 2(iv), 2(v), and 2(I)–2(L)].

1. First stage

We start the calculation of the swimming velocity by obtaining the thrust in the first stage of the swimming stroke, that is, for times $0 \leqslant t \leqslant \tau_p$, where we assume that a single kink propagates from head to tail at velocity $v_0\boldsymbol{\tau}_1$ (see Fig. 3). Using a frame of reference in which the tail appears fixed and instantaneously centered at the location of the kink, the positions of material points in the different domains are given by

$$\mathbf{x}_i = s_i\boldsymbol{\tau}_i, \tag{6}$$

where $i = 1, 2$, $\boldsymbol{\tau}_i$ is the tangent vector along each domain and $s_i \in [0, L_i]$ is the distance moving away from the kink with L_i the length of the corresponding domain (no Einstein summation notation). In this frame of reference, we have $\dot{\mathbf{x}}_1 = \mathbf{0}$ and the deformation velocity of the second domain, $\dot{\mathbf{x}}_2$, can be obtained by noting that after a small interval of time δt, the kink moves along $\boldsymbol{\tau}_1$ a distance $v_0 \delta t$ and the distance from the kink to $\mathbf{x}_2$ increases by $v_0 \delta t$ along $\boldsymbol{\tau}_2$, hence

$$\dot{\mathbf{x}}_2 = v_0(\boldsymbol{\tau}_1 + \boldsymbol{\tau}_2). \tag{7}$$

The hydrodynamic force per unit length is therefore

$$\begin{aligned}\mathbf{f}_i =& \mathbf{f}_i^h - \zeta_\parallel \mathbf{U} \cdot \boldsymbol{\tau}_i \boldsymbol{\tau}_i - \zeta_\perp [\mathbf{U} - \mathbf{U} \cdot \boldsymbol{\tau}_i \boldsymbol{\tau}_i + s_i \boldsymbol{\Omega} \times \boldsymbol{\tau}_i] \\ & - \delta_{i,2} v_0 [\zeta_\parallel (1 + \cos\theta)\boldsymbol{\tau}_i + \zeta_\perp (\boldsymbol{\tau}_1 - \boldsymbol{\tau}_2 \cos\theta)],\end{aligned} \tag{8}$$

where $\mathbf{f}_i^h$ is the hydrodynamic force due to helical rotation (see Sec. II D). Substitution of Eq. (8) in Eqs. (2) and (3) yields

$$\mathbf{F}_i = \mathbf{F}_i^h - \zeta_\perp v_0 L \left[\ell_i (\beta \mathbf{A}_i + \mathbf{B}_i) \cdot \mathbf{u} + \frac{\ell_i^2}{2} \mathbf{C}_i \cdot \boldsymbol{\omega} \right] - \delta_{i,2} \zeta_\perp v_0 L \ell_2 \mathbf{d}_2, \tag{9}$$

$$\mathbf{N}_i = \mathbf{N}_i^h - \zeta_\perp v_0 L^2 \left[\frac{\ell_i^2}{2} \mathbf{C}_i^T \cdot \mathbf{u} + \frac{\ell_i^3}{3} \mathbf{B}_i \cdot \boldsymbol{\omega} \right] - \delta_{i,2} \zeta_\perp v_0 L^2 \frac{\ell_2^2}{2} \mathbf{e}_2, \tag{10}$$

where $\ell_i = L_i/L$, $\mathbf{u} = \mathbf{U}/v_0$, and $\boldsymbol{\omega} = \boldsymbol{\Omega} L/v_0$ are, respectively, the dimensionless length of the domains and linear and angular velocities of the body. We have also made use of the tensors $\mathbf{A}_i = \boldsymbol{\tau}_i \boldsymbol{\tau}_i$ (no Einstein summation notation), $\mathbf{B}_i = \mathbf{1} - \boldsymbol{\tau}_i \boldsymbol{\tau}_i$, $\mathbf{C}_i = \boldsymbol{\epsilon} \cdot \boldsymbol{\tau}_i$, with $\boldsymbol{\epsilon}$ the Levi-Civita pseudotensor, the superscript T denotes transposition, and the vectors $\mathbf{d}_2$ and $\mathbf{e}_2$ are given by

$$\mathbf{d}_2 = \boldsymbol{\tau}_1 + [\beta + \cos\theta(\beta - 1)]\boldsymbol{\tau}_2, \tag{11}$$

$$\mathbf{e}_2 = \boldsymbol{\tau}_2 \times \boldsymbol{\tau}_1. \tag{12}$$

The free-swimming constraint, i.e., $\mathbf{F}_1 + \mathbf{F}_2 = \mathbf{0}$, $\mathbf{N}_1 + \mathbf{N}_2 = \mathbf{0}$, then leads to

$$\mathbf{J}_2 \cdot \begin{pmatrix} \mathbf{u} \\ \boldsymbol{\omega} \end{pmatrix} = \begin{pmatrix} \sum_i \ell_i (\beta \mathbf{A}_i + \mathbf{B}_i) & \frac{1}{2} \sum_i \ell_i^2 \mathbf{C}_i \\ \frac{1}{2} \sum_i \ell_i^2 \mathbf{C}_i^T & \frac{1}{3} \sum_i \ell_i^3 \mathbf{B}_i \end{pmatrix} \cdot \begin{pmatrix} \mathbf{u} \\ \boldsymbol{\omega} \end{pmatrix} = - \begin{pmatrix} \ell_2 \mathbf{d}_2 - \sum_i \hat{\mathbf{F}}_i^h \\ \frac{\ell_2^2}{2} \mathbf{e}_2 - \sum_i \hat{\mathbf{N}}_i^h \end{pmatrix}, \tag{13}$$

where the sums are over $i = 1, 2$ and $\hat{\mathbf{F}}_i^h$ and $\hat{\mathbf{N}}_i^h$ are the dimensionless forces and torques induced by the helical rotation (see Sec. II D).

2. Second stage

During the second stage of the swimming stroke, we need to compute the force per unit length on the third segment; this has tangent vector $\boldsymbol{\tau}_3$, which forms an angle ϑ with $\boldsymbol{\tau}_1$ such that $\boldsymbol{\tau}_1 \cdot \boldsymbol{\tau}_3 = \cos\vartheta = \sin^2\theta(1 - \cos\psi) - 1$, as illustrated in Fig. 4. The position of the material point is given by $\mathbf{x}_3 = D\boldsymbol{\tau}_2 + s_3 \boldsymbol{\tau}_3$, where $s_3 \in [0, L_3]$ is the distance moving away from the second kink. Using an argument similar to the one we used to derive $\dot{\mathbf{x}}_2$, we obtain the velocity of the third domain as

$$\dot{\mathbf{x}}_3 = v_0(\boldsymbol{\tau}_1 + \boldsymbol{\tau}_3), \tag{14}$$

and the hydrodynamic force per unit length is

$$\begin{aligned}\mathbf{f}_3 =& \mathbf{f}_3^h - \zeta_\parallel [\mathbf{A}_3 \cdot \mathbf{U} + v_0(1 + \cos\vartheta)\boldsymbol{\tau}_3 + L_2 \mathbf{A}_3 \cdot \mathbf{C}_2 \cdot \boldsymbol{\Omega}] \\ & - \zeta_\perp [\mathbf{B}_3 \cdot \mathbf{U} + s_3 \mathbf{C}_3 \cdot \boldsymbol{\Omega} + v_0(\boldsymbol{\tau}_1 - \boldsymbol{\tau}_3 \cos\vartheta) + L_2 \mathbf{B}_3 \cdot \mathbf{C}_2 \cdot \boldsymbol{\Omega}].\end{aligned} \tag{15}$$

Hence, the total force and torque on the third portion of the body (measured with respect to $\mathbf{K}$) are

$$\hat{\mathbf{F}}_3 = \hat{\mathbf{F}}_3^h - \left[\ell_3 (\beta \mathbf{A}_3 + \mathbf{B}_3) \cdot \mathbf{u} + \left(\frac{\ell_3^2}{2} \mathbf{C}_3 + \ell_2 \ell_3 (\beta \mathbf{A}_3 + \mathbf{B}_3) \cdot \mathbf{C}_2 \right) \cdot \boldsymbol{\omega} + \ell_3 \mathbf{d}_3 \right], \tag{16}$$

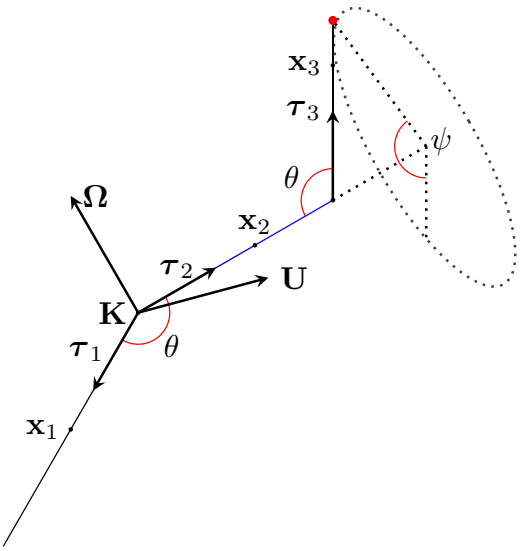

FIG. 4. Second stage of the swimming stroke in the interval $\tau_p \leqslant t \leqslant L/v_0$. We describe the motion in a frame of reference in which the tail appears to be fixed, with instantaneous origin at the location of the kink, $\mathbf{K}(t)$. The body moves with linear velocity $\mathbf{U}(t)$ and rotates with angular velocity $\boldsymbol{\Omega}(t)$. Material points and tangent vectors in each domain axis are denoted by $\mathbf{x}_i$ and $\boldsymbol{\tau}_i$ respectively. It is possible for the third helical domain to be tilted at an angle ψ away from the plane generated by $\boldsymbol{\tau}_1$ and $\boldsymbol{\tau}_2$.

$$\hat{\mathbf{N}}_3 = \hat{\mathbf{N}}_3^h - \left[\frac{\ell_3^2}{2}\mathbf{C}_3^T\cdot\mathbf{u} + \left(\frac{\ell_3^3}{3}\mathbf{B}_3 + \frac{\ell_2\ell_3^2}{2}\mathbf{C}_3^T\cdot\mathbf{C}_2\right)\cdot\boldsymbol{\omega} + \frac{\ell_3^2}{2}\mathbf{e}_3 - \ell_2\mathbf{C}_2^T\cdot\left(\hat{\mathbf{F}}_3 - \hat{\mathbf{F}}_3^h\right)\right], \tag{17}$$

where we have defined the vectors $\mathbf{d}_3 = \boldsymbol{\tau}_1 + [\beta + \cos\vartheta(\beta-1)]\boldsymbol{\tau}_3$ and $\mathbf{e}_3 = \boldsymbol{\tau}_3\times\boldsymbol{\tau}_1$ as in Eqs. (11) and (12). Applying the free-swimming conditions, $\sum_i \mathbf{F}_i = \mathbf{0}$, $\sum_i \mathbf{N}_i = \mathbf{0}$, we now obtain

$$(\mathbf{J}_3 + \mathbf{K}_3)\cdot\begin{pmatrix}\mathbf{u}\\ \boldsymbol{\omega}\end{pmatrix} = -\begin{pmatrix}\ell_2\mathbf{d}_2 + \ell_3\mathbf{d}_3 - \sum_i \hat{\mathbf{F}}_i^h\\ \frac{\ell_2^2}{2}\mathbf{e}_2 + \frac{\ell_3^2}{2}\mathbf{e}_3 + \ell_2\ell_3\boldsymbol{\tau}_2\times\mathbf{d}_3 - \sum_i \hat{\mathbf{N}}_i^h\end{pmatrix}, \tag{18}$$

where the matrix $\mathbf{J}_3$ is as in Eq. (13), but now with sums over all three indices $i = 1, 2, 3$, and where

$$\mathbf{K}_3 = \ell_2\ell_3\begin{pmatrix}\mathbf{0} & (\beta\mathbf{A}_3 + \mathbf{B}_3)\cdot\mathbf{C}_2\\ \mathbf{C}_2^T\cdot(\beta\mathbf{A}_3 + \mathbf{B}_3) & \ell_3\left(\mathbf{C}_2^T\cdot\mathbf{C}_3\right)^S + \ell_2\mathbf{C}_2^T\cdot(\beta\mathbf{A}_3 + \mathbf{B}_3)\cdot\mathbf{C}_2\end{pmatrix}, \tag{19}$$

where the superscript S denotes symmetrization of the given tensor, i.e., $\mathbf{Q}^S = (\mathbf{Q} + \mathbf{Q}^T)/2$ for any tensor $\mathbf{Q}$.

3. Third stage

Using the symmetry of the stroke between the first and the third stages, the linear and angular velocities in the third stage of the motion can be obtained from Eq. (13) with the identification $\{\boldsymbol{\tau}_1, \ell_1\} \mapsto \{-\boldsymbol{\tau}_2, \ell_2\}$ and $\{\boldsymbol{\tau}_2, \ell_2\} \mapsto \{\boldsymbol{\tau}_3, \ell_3\}$. In this case, the frame of reference is chosen so that the second domain appears fixed and is centered at the location of the second kink. Note that the information about the orientation of the cell, carried by $\boldsymbol{\tau}_1$, is not lost since, as the kink angle θ is fixed, the same information is contained in the vector $\boldsymbol{\tau}_2$.

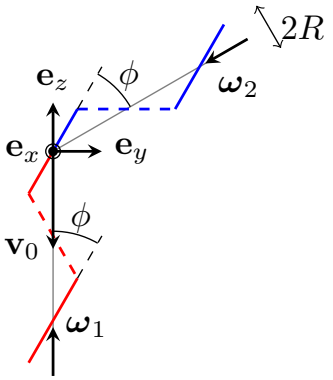

FIG. 5. Side view of the helical domains in the vicinity of the kink. The bottom left segment (red) represents the centerline of a right-handed helix, while the top right segment (blue) represents the centerline of a left-landed helix. Both helices have the same radius R and pitch angle ϕ. The different domains rotate in opposite directions at angular velocities ω_1 and ω_2.

D. Helical geometry: Coarse-grained model

1. Helical propulsion

As the kink propagates along the bacterial body, as explained above the domains with different handedness rotate in opposite senses and therefore both propel the bacteria in the same direction. To account for the hydrodynamic effect of helical propulsion, we follow the treatment used by Wada and Netz [22]. We consider a coarse-grained model in which we ignore end effects so that the hydrodynamic force per unit length acting on any of the helical domains is the same as the one that acts on an infinite helix rotating around its axis. Following resistive-force theory, we know that the swimming velocity U^h of an infinite helix of radius R and pitch angle ϕ rotating with angular velocity ω_φ around its axis is given by [22]

$$U^h(\omega_\varphi) = \frac{R(1-\beta^h)\sin\phi\cos\phi}{(\beta^h + (1-\beta^h)\sin^2\phi)}\omega_\varphi, \tag{20}$$

where β^h is the ratio of the parallel to the perpendicular drag coefficient of the slender filament making up the helix. The hydrodynamic force acting on each of the individual helical domains and due to the rotation of the helical domain therefore has magnitude $|\mathbf{F}_i^h| \simeq \zeta_\parallel L_i U^h$, acting along the helical axis.

We next need to determine the angular velocity at which the domains rotate. Using a frame of reference in which the junction point (the kink) is fixed and the domains appear to grow and shrink, respectively, we parametrize the helical domains explicitly as (see Fig. 5)

$$\frac{\mathbf{x}_1^h}{R} = \cos\varphi_1\mathbf{e}_x - \sin\varphi_1\mathbf{e}_y - \frac{\varphi_1}{\tan\phi}\mathbf{e}_z, \tag{21}$$

$$\frac{\mathbf{x}_2^h}{R} = \cos\varphi_2\mathbf{e}_x + \left(\frac{\varphi_2}{\tan\phi}\sin(2\phi) - \sin\varphi_2\cos(2\phi)\right)\mathbf{e}_y + \left(\frac{\varphi_2}{\tan\phi}\cos(2\phi) + \sin\varphi_2\sin(2\phi)\right)\mathbf{e}_z, \tag{22}$$

where $\varphi_i = \Phi_i(t) - \tilde{\varphi}_i = \Phi_{i_0} + (-1)^{i-1}\omega_{\varphi_i}t - \tilde{\varphi}_i$ with $\tilde{\varphi}_i \in [0, \Phi_i(t)]$, and $L_{i_0} = \Phi_{i_0}/\tan\phi$ is the initial length of the domains. Hence the angular velocity at φ_i is $\dot{\varphi}_i = (-1)^{i-1}\omega_{\varphi_i}$. By continuity at the junction point ($\varphi_i = 0$) we have

$$\mathbf{e}_z \cdot \left(\dot{\mathbf{x}}_1^h + \dot{\mathbf{x}}_2^h\right) = -R\left[\frac{\omega_{\varphi_1}}{\tan\phi} + \omega_{\varphi_2}\left(\frac{\cos(2\phi)}{\tan\phi} + \sin(2\phi)\right)\right] = -\frac{R(\omega_{\varphi_1} + \omega_{\varphi_2})}{\tan\phi}. \tag{23}$$

During the first stage of the motion, in a small interval of time δt the kink moves a distance $(-1)^{i-1}R\omega_{\varphi_i}\cot\phi\delta t$ along the axis of the corresponding helical domains. As the kink travels at speed v_0 this same distance must be equal to $v_0\delta t$. Thus, we obtain the kinematic relationship $R(\omega_{\varphi_1}+\omega_{\varphi_2})=2v_0\tan\phi$. Furthermore, the torque on each of the domains is proportional to their arclength and their angular velocity, hence by torque balance we have $\omega_1 L_1 \simeq \omega_2 L_2$. Combining this with Eq. (20) and Eq. (23) leads to the helical hydrodynamic forces on each domain for the first stage of the swimming stroke,

$$\hat{\mathbf{F}}_i^h = (-1)^i \frac{2\beta(1-\beta^h)\cos^2(\theta/2)}{\beta^h+(1-\beta^h)\cos^2(\theta/2)}\ell_2(1-\ell_2)\boldsymbol{\tau}_i = \beta f(\beta^h,\theta)\ell_2(1-\ell_2)(-1)^i\boldsymbol{\tau}_i, \tag{24}$$

with $i=1,2$ (no Einstein summation). Here we have used the condition $\ell_1+\ell_2=1$, with $\ell_i = L_i/L$, and the continuity condition $2\phi=\pi-\theta$ (see Fig. 5).

In the second stage of the swimming stroke, the analysis is similar but the torque condition is now written $\omega_1(\ell_1+\ell_3)=\omega_2\ell_2$ instead, hence $\hat{\mathbf{F}}_1^h = -f\beta\ell_1 d\boldsymbol{\tau}_1$, $\hat{\mathbf{F}}_2^h = f\beta(1-d)d\boldsymbol{\tau}_2$, and $\hat{\mathbf{F}}_3^h = -f\beta\ell_3 d\boldsymbol{\tau}_1$.

Finally, the configuration in the third stage is analogous to that in the first stage discussed above, but now with $\hat{\mathbf{F}}_2^h = \beta f\ell_2(1-\ell_2)\boldsymbol{\tau}_1$ and $\hat{\mathbf{F}}_3^h = -\beta f\ell_2(1-\ell_2)\boldsymbol{\tau}_1$.

2. Effective drag ratio

A slender filament in a viscous fluid has a drag ratio $\beta_\infty = 1/2$ in the asymptotic limit of a small cross-sectional length relative to the filament length. Our effective rod model has a drag ratio β that captures the effective ratio of tangential to perpendicular drag and whose value should of course depend on the geometry of the helical body. In order to include more detail of the helical geometry of *Spiroplasma* in our calculation, we can derive the values of the parallel and perpendicular drag coefficients by considering the hydrodynamic forces acting on an infinitely long helix that is translating along its axis and perpendicular to it, respectively. We parametrize the material points on the helix as

$$\mathbf{x}^h = \mathbf{e}_x R\cos\varphi + \mathbf{e}_y R\sin\varphi + \mathbf{e}_z\frac{R\varphi}{\tan\phi}, \tag{25}$$

where the angle φ is related to the arclength by $s = R\varphi/\sin\phi$. The unit tangent vector to the helix centerline $\boldsymbol{\tau}^h$ is obtained by taking the derivative with respect to the arclength, and thus

$$\boldsymbol{\tau}^h = -\mathbf{e}_x\sin\varphi\sin\phi + \mathbf{e}_y\cos\varphi\sin\phi + \mathbf{e}_z\cos\phi. \tag{26}$$

We first calculate the force that acts on the helix when it moves along its axis at speed V. Using resistive-force theory we obtain the hydrodynamic force density

$$\mathbf{f}_a^{\parallel} = -[\zeta_\perp^h(V\mathbf{e}_z - V\boldsymbol{\tau}^h\boldsymbol{\tau}^h\cdot\mathbf{e}_z) + \zeta_\parallel^h V\boldsymbol{\tau}^h\boldsymbol{\tau}^h\cdot\mathbf{e}_z] = -[(\zeta_\parallel^h-\zeta_\perp^h)V\cos\phi\boldsymbol{\tau}^h + \zeta_\perp^h V\mathbf{e}_z], \tag{27}$$

where $\zeta_\perp^h$ and $\zeta_\parallel^h$ are the drag coefficients perpendicular and parallel to the centerline of the helical filament. By definition, the coarse-grained parallel drag coefficient is the ratio between longitudinal force per unit length and speed, i.e.,

$$\zeta_\parallel \simeq -\frac{1}{LV}\int_0^L \mathbf{f}_a^{\parallel}\cdot\mathbf{e}_z\,\mathrm{d}s = \zeta_\parallel^h\cos^2\phi + \zeta_\perp^h\sin^2\phi. \tag{28}$$

Similarly, to derive the perpendicular drag coefficient we calculate the hydrodynamic force density acting on the helix when it moves perpendicular to the helical axis as

$$\begin{aligned}\mathbf{f}_a^{\perp} &= -[\zeta_\perp^h(V\mathbf{e}_x - V\boldsymbol{\tau}^h\boldsymbol{\tau}^h\cdot\mathbf{e}_x) + \zeta_\parallel^h V\boldsymbol{\tau}^h\boldsymbol{\tau}^h\cdot\mathbf{e}_x]\\ &= -[-(\zeta_\parallel^h-\zeta_\perp^h)V\sin\varphi\sin\phi\boldsymbol{\tau}^h + \zeta_\perp^h V\mathbf{e}_x].\end{aligned} \tag{29}$$

The coarse-grained perpendicular drag coefficient is thus given by

$$\begin{aligned}\zeta_\perp &\simeq -\frac{1}{LV}\int_0^L \mathbf{f}_a^\perp \cdot \mathbf{e}_x \, \mathrm{d}s \\ &= \frac{(\zeta_\parallel^h - \zeta_\perp^h)\sin^2\phi}{L}\int_0^L \sin^2\varphi(s)\,\mathrm{d}s + \zeta_\perp^h \\ &= \frac{\zeta_\parallel^h}{2}\sin^2\phi + \frac{\zeta_\perp^h}{2}(1+\cos^2\phi). \end{aligned} \tag{30}$$

Hence the drag ratio for the coarse-grained helical body is obtained as

$$\beta = \frac{\zeta_\parallel}{\zeta_\perp} = 2\frac{\beta^h \sin^2\phi + \cos^2\phi}{\beta^h \sin^2\phi + (1+\cos^2\phi)}. \tag{31}$$

Assuming an asymptotically slender helical filament, we may assume $\beta^h = \zeta_\parallel^h/\zeta_\perp^h = 1/2$. As a result, the effective helix drag ratio β is obtained as a function of $\theta \equiv \pi - 2\phi$ as

$$\beta = 2\left(\frac{3+\cos\theta}{7-\cos\theta}\right). \tag{32}$$

In the case where $\theta = \pi$, the helix becomes a straight filament ($\phi = 0$) and we recover $\beta = 1/2$ as expected. At the other extreme, $\theta = 0$, the helix becomes a circle and $\beta = 4/3$; indeed it is easier to move this filament in the plane that contains it than in the perpendicular direction.

III. PLANAR MOTION, NO HELICAL GEOMETRY

We first analyze the model ignoring the helical geometry (i.e., we ignore the contributions from $\mathbf{F}_i^h$ and $\mathbf{N}_i^h$). Given that previous numerical results have shown that the swimming trajectories follow almost-straight lines [22], we also assume that the cell motion is planar. We demonstrate that, under these assumptions, the orientation of the cell body does not change after one period of the swimming stroke. This allows us to define an effective swimming speed and a hydrodynamic efficiency with no ambiguity.

A. Kinematics

We start by considering the case in which the model cell moves in a plane, i.e., $\psi = 0$ or $\boldsymbol{\tau}_3 = -\boldsymbol{\tau}_1$. In this case we can define normal vectors $\boldsymbol{\nu}_i \equiv \hat{\mathbf{z}} \times \boldsymbol{\tau}_i$, where $(\sin\theta)\hat{\mathbf{z}} = \boldsymbol{\tau}_1 \times \boldsymbol{\tau}_2$. Defining $\boldsymbol{\tau} \equiv \boldsymbol{\tau}_1$, $\boldsymbol{\nu} \equiv \boldsymbol{\nu}_1$, we have $\boldsymbol{\tau}_2 = \cos\theta\boldsymbol{\tau} + \sin\theta\boldsymbol{\nu}$ and $\boldsymbol{\nu}_2 = -\sin\theta\boldsymbol{\tau} + \cos\theta\boldsymbol{\nu}$, hence we can express Eqs. (13) and (18) for the components of the linear and angular velocities parallel and perpendicular to $\boldsymbol{\tau}_1$ as

$$\left(\tilde{\mathbf{J}} + \mathbb{I}_{\ell_2=d}\tilde{\mathbf{K}}\right)\cdot\begin{pmatrix} u_\tau \\ u_\nu \\ \omega \end{pmatrix} = \begin{pmatrix} -\ell_2[1+(\beta-(1-\beta)\cos\theta)\cos\theta] \\ -\ell_2(\beta-(1-\beta)\cos\theta)\sin\theta \\ \ell_2^2\sin\theta/2 \end{pmatrix}, \tag{33}$$

where $d = v_0\tau_p/L$ and $\mathbb{I}_{x=y}$ is an indicator function, which is 1 if $x = y$ and 0 otherwise. The symmetric matrices $\tilde{\mathbf{J}}$ and $\tilde{\mathbf{K}}$ have components

$$\tilde{J}_{11} = \ell_2(1-\beta)\sin^2\theta + \beta, \tag{34}$$

$$\tilde{J}_{12} = -\ell_2(1-\beta)\sin\theta\cos\theta, \tag{35}$$

$$\tilde{J}_{13} = -\ell_2^2\sin\theta/2, \tag{36}$$

$$\tilde{J}_{22} = 1 - \ell_2(1-\beta)\sin^2\theta, \tag{37}$$

$$\tilde{J}_{23} = \left[\ell_1^2 + \ell_2^2 \cos\theta\right]/2, \tag{38}$$

$$\tilde{J}_{33} = \left[\ell_1^3 + \ell_2^3\right]/3, \tag{39}$$

while the nonzero components of $\tilde{\mathbf{K}}$ are

$$\tilde{K}_{13} = -d\ell_3\beta \sin\theta, \tag{40}$$

$$\tilde{K}_{23} = \ell_3(d\cos\theta - \ell_3/2), \tag{41}$$

$$\tilde{K}_{33} = \ell_3\left[\ell_3^2/3 + d^2\cos^2\theta(1-\beta)\right] + \ell_3[\beta d^2 - d\ell_3\cos\theta]. \tag{42}$$

Note that due to the normalization condition $\ell_1 + \ell_2 + \ell_3 = 1$, the components of $\tilde{\mathbf{J}}$ in the second stage of the swimming stroke are the same as those in the first stage if we simply take $\ell_2 = d$. Further, as mentioned above, the linear and angular velocities in the third stage can be obtained from those in the first stage of the motion. Therefore we only need to solve Eq. (33) for $\{u_\tau, u_\nu, \omega\}$ and integrate to obtain the angular and linear displacements. Solving Eq. (33) in the first and second stages we find the angular and linear velocities in the body frame, $\{u_\tau^{(j)}, u_\nu^{(j)}, \omega^{(j)}\}$, where the superscript denotes the swimming stage, i.e., $j = 1, 2$. Assuming that at the beginning of each stage of the motion $\boldsymbol{\tau}^{(j)} = -\hat{\mathbf{y}}$ and denoting by $\alpha^{(j)}(\ell)$ the angle that $\boldsymbol{\tau}^{(j)}$ makes with the $-y$ axis at $\ell_2 = \ell$ for $j = 1$ or $\ell_3 = \ell$ for $j = 2$, we have $\boldsymbol{\tau}(\alpha) = \sin\alpha\hat{\mathbf{x}} - \cos\alpha\hat{\mathbf{y}}$, $\boldsymbol{\nu}(\alpha) = \cos\alpha\hat{\mathbf{x}} + \sin\alpha\hat{\mathbf{y}}$, and the Cartesian components of the velocity are

$$u_x = u_\tau \sin\alpha + u_\nu \cos\alpha, \tag{43}$$

$$u_y = -u_\tau \cos\alpha + u_\nu \sin\alpha, \tag{44}$$

where we omit the superscript for simplicity. The angular displacement $\alpha^{(j)}$ is obtained by integrating the angular velocity $\omega^{(j)}$ in time, and therefore

$$\alpha^{(1)}(\ell) = \int_0^\ell \omega^{(1)}(\ell_2)\,\mathrm{d}\ell_2, \tag{45}$$

$$\alpha^{(2)}(\ell) = \alpha^{(1)}(d) + \int_0^\ell \omega^{(2)}(\ell_3)\,\mathrm{d}\ell_3. \tag{46}$$

In order to obtain the displacement $\mathbf{x}_T = \mathbf{X}_T/L$, we first calculate the position of the head during the first stage at $\ell_2 = \ell$, i.e., $\mathbf{h}^{(1)}(\ell) = \mathbf{k}^{(1)}(\ell) + \ell\boldsymbol{\tau}^{(1)}(\ell)$. Here $\mathbf{h}^{(1)}$ is the dimensionless position of the head and $\mathbf{k}^{(1)}$ that of the kink, which is given by

$$\mathbf{k}^{(1)}(\ell) = \int_0^\ell [\mathbf{u}^{(1)}(\ell_2) + \boldsymbol{\tau}^{(1)}(\ell_2)]\,\mathrm{d}\ell_2. \tag{47}$$

The position of the head during the second stage at $\ell_3 = \ell$ is

$$\mathbf{h}^{(2)}(\ell) = \mathbf{k}^{(2)}(\ell) + d\boldsymbol{\tau}_2^{(2)}(\ell) - (1-d)\boldsymbol{\tau}^{(2)}(\ell), \tag{48}$$

where $\mathbf{k}^{(2)}$ is the position of the first kink and is given by

$$\mathbf{k}^{(2)}(\ell) = \mathbf{k}^{(1)}(d) + \int_0^\ell [\mathbf{u}^{(2)}(\ell_3) + \boldsymbol{\tau}^{(2)}(\ell_3)]\,\mathrm{d}\ell_3. \tag{49}$$

It only remains to calculate the displacement of the head in the last stage of the motion $\mathbf{h}^{(3)}$. Using a symmetry argument, we show below that this displacement is the same as that of the tail in the first stage.

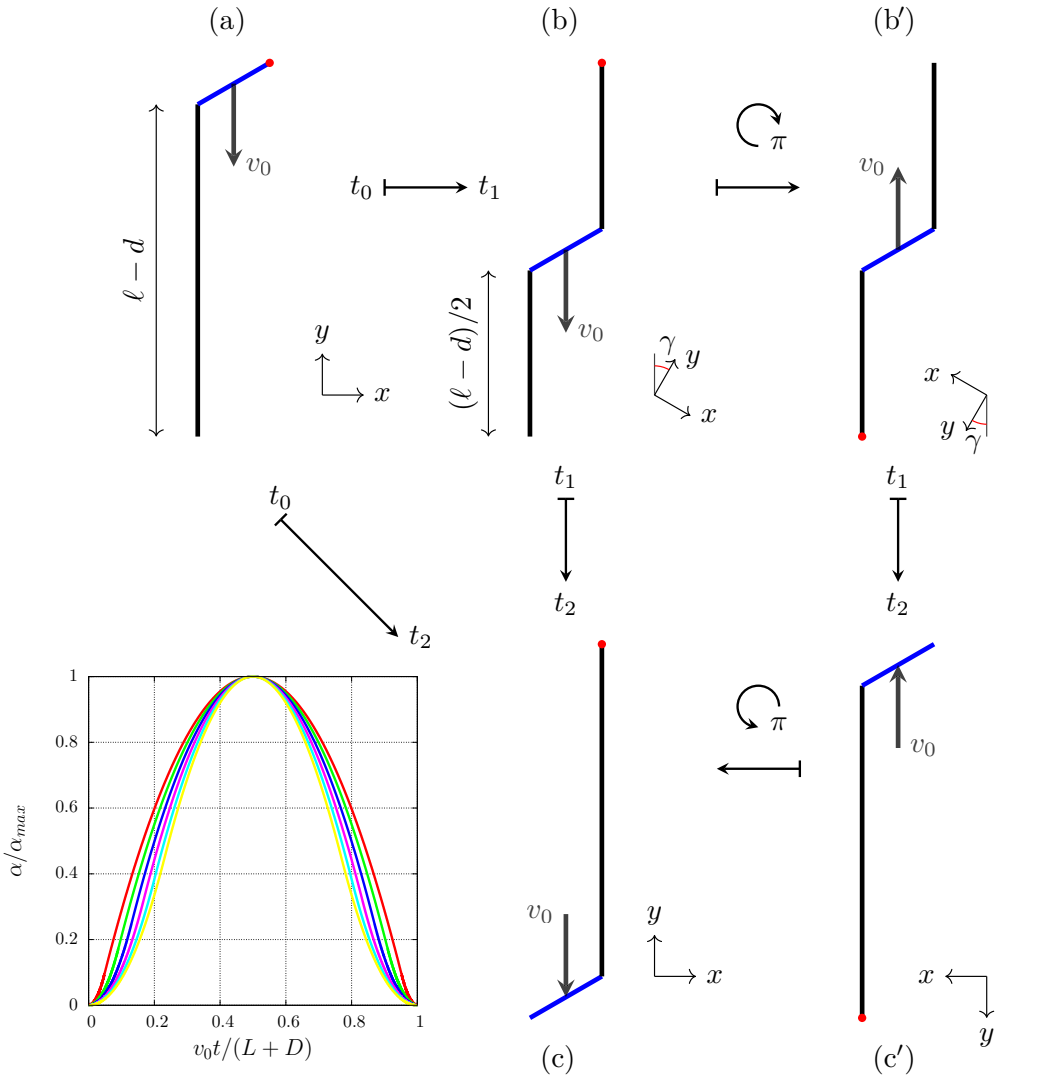

FIG. 6. Total angular displacement during the periodic stroke. Due to the time reversibility of Stokes flow, the angular displacement γ during the first half of the stroke—i.e., going from configuration (a) to configuration (b)—is the opposite of that occurring during the second half—i.e., going from (b′) to (c′) or, equivalently, from (b) to (c). Hence the total angular displacement during the complete stroke vanishes. Bottom-left inset: Instantaneous angular displacements for $\theta = 110^\circ$, $\beta = 1/2$, and values of d ranging from $d = 0.05$ (top) to $d = 0.3$ (bottom) in increments of 0.05 as obtained by a numerical integration of Eq. (33) using a midpoint Euler method.

B. No net rotation

Under our modeling assumptions, we note that the swimming stroke is symmetric under a rotation by 180° in the plane of motion and a time reversal $t \mapsto T - t$ (see illustration in Fig. 6). Given that Stokes flows are reversible in time, changing the signs of the forces and torques acting on the body, or, equivalently, reversing time, changes the signs of the linear and angular velocity. Therefore, the angular displacement γ in the first half of the stroke [Figs. 6(a) and 6(b)] is the opposite of that obtained by reversing the propagation of the kink [Figs. 6(b′) and 6(c′)]. By

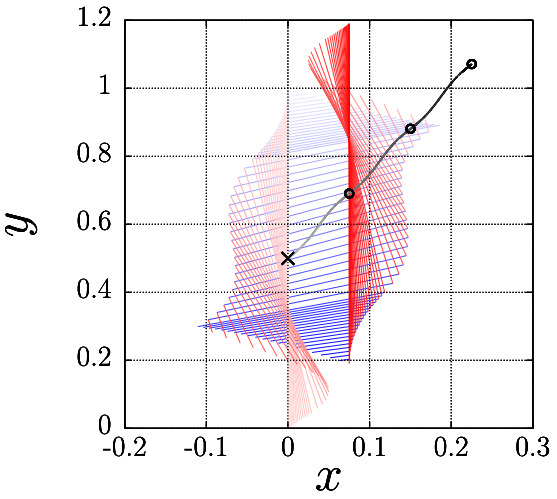

FIG. 7. Snapshots of swimming trajectory for the case $d = 0.25$, with darker shades denoting an increase in time. The instantaneous location of the center of mass is represented by the solid black line. The trajectory over three strokes is shown. The shades represent the deformation of the cell body during the stroke (only the first stroke is shown), with the axis of the right-handed domain(s) shown in red and that of the left-handed domain represented in blue. The cross indicates the initial position of the center of mass, and the circles its position at the end of a stroke (see Movie 1 in Supplemental Material [28]).

the symmetry of the motion this is the same angular displacement as that of the second half of the stroke [Figs. 6(b) and 6(c)]. Therefore by reversibility of the Stokes equations, the total angular displacement at the end of the swimming stroke vanishes. The fact that the cell orientation does not change after one complete cycle is confirmed by the numerical solutions of Eq. (45) and Eq. (46) shown in the bottom-left inset in Fig. 6 and displaying the angular displacement as a function of time for different values of the interkink distance.

Using the same symmetry argument, we deduce that the total displacement during the third stage of the motion is the same as the total displacement of the tail in the first stage. The latter is given by $\mathbf{t}^{(1)}(d) = \mathbf{k}^{(1)}(d) + (1-d)\boldsymbol{\tau}^{(1)}(d) - \mathbf{t}^{(1)}(0)$. Therefore, after one stroke, the total linear and angular displacements are $\mathbf{x}_T = \mathbf{h}^{(2)}(1-d) + \mathbf{t}^{(1)}(d)$ [with $\mathbf{h}(t=0) = \mathbf{0}$] and $\phi_T = 0$, respectively.

We illustrate in Fig. 7 the trajectory of the center of mass of the cell (solid black line), obtained by numerical solution of Eq. (33), in the case $d = 0.25$. The time evolution of the deformation is represented by the red (right-handed part of the cell) and blue (left-handed) shades, while the circles denote the end of each stroke and the cross the initial position of the center of mass. Darker shades denote an increase in time. The kink travels in the negative y direction, while the cell swims in the positive y direction (see Movie 1 in the Supplemental Material [28]).

C. Swimming speed and efficiency

Since the body orientation does not change after one swimming stroke, we may define an effective swimming speed v_s as the ratio of the total distance traveled in one cycle to the period of the stroke, i.e.,

$$v_s^2 \equiv \frac{L^2}{T^2}\left(x_T^2 + y_T^2\right) = \frac{v_k^2 \sin^2(\theta/2)}{(1+d)^2}\left(x_T^2 + y_T^2\right). \tag{50}$$

We may also compute the average rate of energy dissipation (i.e., power) during one swimming stroke as

$$\dot{W} = \frac{1}{T}\int_0^T \int_0^L \mathbf{f}(s,t)\cdot\mathbf{v}(s,t)\,\mathrm{d}s\,\mathrm{d}t, \tag{51}$$

where the hydrodynamic force density $\mathbf{f}$ is given in Eq. (1) and where $\mathbf{v}$ is the instantaneous velocity of each helical domain axis. We can split the time integral from Eq. (51) in three parts, $\dot{W} = \dot{W}_1 + \dot{W}_2 + \dot{W}_3$, with each one corresponding to the three different stages of the swimming motion discussed in Sec. II C. By symmetry of the stroke, we have $\dot{W}_1 = \dot{W}_3$ and thus $\dot{W} = 2\dot{W}_1 + \dot{W}_2$. Dividing by $\zeta_\perp L v_0^2$, the nondimensional rates of energy dissipation in each stage are given by

$$\hat{\dot{W}}_1 = \frac{1}{1+d}\left[\int_0^d \int_0^{1-\ell_2} \mathbf{u}_1^{(1)}(\ell_2,\ell)\cdot\left(\beta\mathbf{A}_1^{(1)} + \mathbf{B}_1^{(1)}\right)\cdot\mathbf{u}_1^{(1)}(\ell_2,\ell)\mathrm{d}\ell\mathrm{d}\ell_2 + \int_0^d \int_0^{\ell_2} \mathbf{u}_2^{(1)}(\ell_2,\ell)\cdot\left(\beta\mathbf{A}_2^{(1)} + \mathbf{B}_2^{(1)}\right)\cdot\mathbf{u}_2^{(1)}(\ell_2,\ell)\mathrm{d}\ell\mathrm{d}\ell_2\right], \tag{52}$$

$$\begin{aligned}\hat{\dot{W}}_2 = \frac{1}{1+d}\Bigg[&\int_0^{1-d} \int_0^{1-d-\ell_3} \mathbf{u}_1^{(2)}(\ell_3,\ell)\cdot\left(\beta\mathbf{A}_1^{(2)} + \mathbf{B}_1^{(2)}\right)\cdot\mathbf{u}_1^{(2)}(\ell_3,\ell)\mathrm{d}\ell\mathrm{d}\ell_3 \\ &+ \int_0^{1-d} \int_0^{d} \mathbf{u}_2^{(2)}(\ell_3,\ell)\cdot\left(\beta\mathbf{A}_2^{(2)} + \mathbf{B}_2^{(2)}\right)\cdot\mathbf{u}_2^{(2)}(\ell_3,\ell)\mathrm{d}\ell\mathrm{d}\ell_3 \\ &+ \int_0^{1-d} \int_0^{\ell_3} \mathbf{u}_3^{(2)}(\ell_3,\ell)\cdot\left(\beta\mathbf{A}_1^{(2)} + \mathbf{B}_1^{(2)}\right)\cdot\mathbf{u}_3^{(2)}(\ell_3,\ell)\mathrm{d}\ell\mathrm{d}\ell_3\Bigg],\end{aligned} \tag{53}$$

where $\mathbf{A}_i^{(j)} = \boldsymbol{\tau}^{(j)}\boldsymbol{\tau}^{(j)}$ and

$$\mathbf{u}_1^{(j)}(\ell',\ell) = u_\tau^{(j)}(\ell')\boldsymbol{\tau}^{(j)}(\ell') + \left(u_\nu^{(j)}(\ell') + \omega^{(j)}(\ell')\ell\right)\boldsymbol{\nu}^{(j)}(\ell'), \tag{54}$$

$$\begin{aligned}\mathbf{u}_2^{(j)}(\ell',\ell) = &\left(u_\tau^{(j)}(\ell') - \omega^{(j)}(\ell')\ell\sin\theta + 1 + \cos\theta\right)\boldsymbol{\tau}^{(j)}(\ell') \\ &+ \left(u_\nu^{(j)}(\ell') + \omega^{(j)}(\ell')\ell\cos\theta + \sin\theta\right)\boldsymbol{\nu}^{(j)}(\ell'),\end{aligned} \tag{55}$$

$$\mathbf{u}_3^{(j)}(\ell',\ell) = \left(u_\tau^{(j)}(\ell') - \omega^{(j)}(\ell')d\sin\theta\right)\boldsymbol{\tau}^{(j)}(\ell') + \left(u_\nu^{(j)}(\ell') + \omega^{(j)}(\ell')(d\cos\theta - \ell)\right)\boldsymbol{\nu}^{(j)}(\ell'). \tag{56}$$

Here the subscript $j = 1, 2$ denotes the swimming stage and $(u_\tau^{(j)}, u_\nu^{(j)}, \omega^{(j)})$ are obtained by solving Eq. (33). As is commonly done in low-Reynolds-number swimming, we compare the dissipated power in one stroke, against the power dissipated by a straight model cell of length L dragged at speed v_s along its axis, i.e., $\hat{W}_0 = \beta(v_s/v_0)^2$. The efficiency is then defined as the ratio

$$\eta \equiv \frac{\hat{W}_0}{\hat{W}} = \frac{\beta v_s^2}{v_0^2(2\hat{W}_1 + \hat{W}_2)}. \tag{57}$$

In the next section we include the additional forces and torques resulting from the helical geometry modeled at the coarse-grained level. We show that the cell does not rotate in that case either and therefore both Eq. (50) and Eq. (57) will remain applicable.

IV. PLANAR MOTION, BISTABLE HELIX

Now we turn our attention to the coarse-grained model in which we include the details of the helical geometry. The symmetry argument we used to deduce that the bacterium does not change its orientation after one stroke remains valid when we add the forces due to the rotation of the helical domains. Indeed as represented in Fig. 8, the swimming stroke is still symmetric under a rotation by 180° and time reversal. Therefore, for every configuration with velocities $\{\mathbf{U}, \boldsymbol{\Omega}\}$ at time t, there is

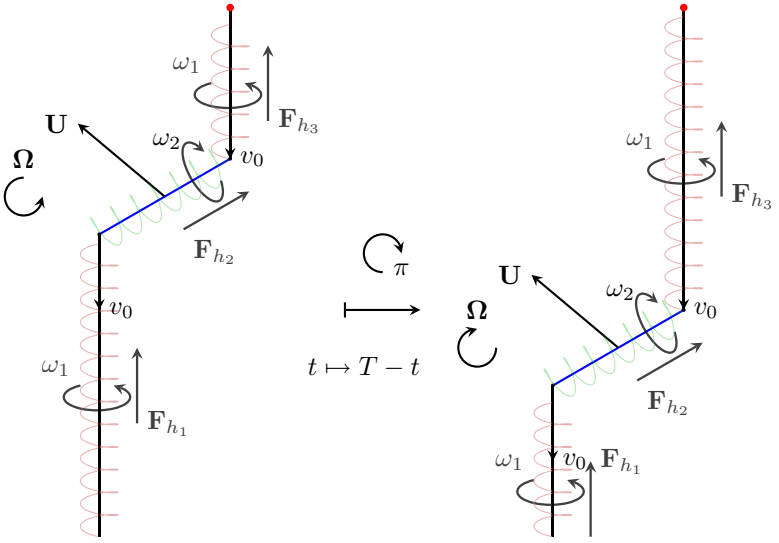

FIG. 8. The swimming gait remains symmetric even when the helical domains are included. Given a configuration with instantaneous linear and angular velocity $\{\mathbf{U}, \mathbf{\Omega}\}$ at time t it is possible to find the linear and angular velocities of the configuration at time $T - t$, where T is the period of the stroke, by rotating one-half revolution and reversing the signs of the instantaneous forces.

a corresponding configuration with velocities $\{\mathbf{U}, -\mathbf{\Omega}\}$ at time $T - t$, hence the orientation remains unchanged after one stroke.

From Eq. (24) and the condition $\ell_1 + \ell_2 + \ell_3 = 1$, the extra forces and torques due to the helical rotation are given by

$$\sum_i \hat{\mathbf{F}}_i^h = \beta f(\theta)(1-\ell_2)\ell_2[\boldsymbol{\tau}(\cos\theta - 1) + \boldsymbol{\nu}\sin\theta], \tag{58}$$

$$\sum_i \hat{\mathbf{N}}_i^h = \beta f(\theta)\ell_2^2\ell_3 \sin\theta \hat{\mathbf{z}} \tag{59}$$

in all three swimming stages. These extra terms enter on the right-hand side of Eq. (33) and therefore only $\{u_\tau, u_\nu, \omega\}$ are modified. Hence, Eqs. (43)–(49) and the expressions for the swimming speed and the dissipated energy, Eq. (50) and Eq. (51), respectively, remain unchanged. Note that both Eq. (52) and Eq. (53) are also valid in the case in which we consider helical propulsion. There is, however, an extra contribution to the dissipated energy that comes from the product $\mathbf{f}^h \cdot \mathbf{v}$. The total dissipated energy therefore becomes $\hat{W}^{(h)} = 2\hat{W}_1 + \hat{W}_2 + 2\hat{W}_1^{(h)} + \hat{W}_2^{(h)}$, where

$$\hat{W}_1^{(h)} = \frac{\beta f}{1+d}\int_0^d \left[\int_0^{1-\ell_2} -\ell_2 \boldsymbol{\tau}^{(1)}(\ell_2)\cdot\mathbf{u}_1^{(1)}(\ell_2,\ell)\,\mathrm{d}\ell + \int_0^{\ell_2} \ell_1 \boldsymbol{\tau}_2^{(1)}(\ell_2)\cdot\mathbf{u}_2^{(1)}(\ell_2,\ell)\,\mathrm{d}\ell\right]\mathrm{d}\ell_2, \tag{60}$$

$$\hat{W}_2^{(h)} = \frac{\beta f}{1+d}\int_0^{1-d}\left[\int_0^{1-d-\ell_3} -d\boldsymbol{\tau}^{(2)}(\ell_3)\cdot\mathbf{u}_1^{(2)}(\ell_3,\ell)\,\mathrm{d}\ell + \int_0^d (1-d)\boldsymbol{\tau}_2^{(2)}(\ell_3)\cdot\mathbf{u}_2^{(2)}(\ell_3,\ell)\,\mathrm{d}\ell - \int_0^{\ell_3} d\boldsymbol{\tau}^{(2)}(\ell_3)\cdot\mathbf{u}_3^{(2)}(\ell_3,\ell)\,\mathrm{d}\ell\right]\mathrm{d}\ell_3. \tag{61}$$

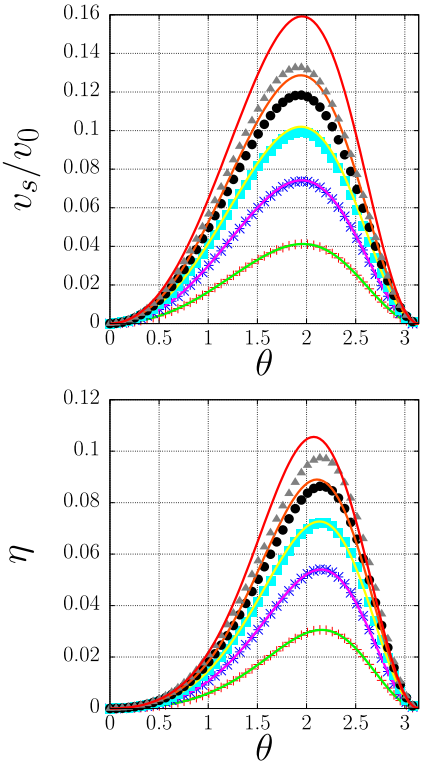

FIG. 9. Average swimming speed (top) and efficiency (bottom) of the model *Spiroplasma* as a function of the kink angle, θ. Top: Comparison between the full numerical solution (symbols) and the asymptotic expansion (line) for the swimming speed, Eq. (64), with d increasing from 0.05 to 0.25 from bottom to top in steps of 0.05. Bottom: Comparison between the full numerical solution (symbols) and the asymptotic expansion (line), for the efficiency, Eq. (66), for the same values of d. In both cases the dependence on d is weak.

V. ASYMPTOTIC AND NUMERICAL RESULTS

We now explore the results of our models, compare the predictions of asymptotic expansions to numerical simulations, and predict the optimal cell shape. Since the body does not reorient during each stroke, in order to obtain the swimming speed, we only need to calculate the linear displacement, $\mathbf{x}_T$. It is possible, in principle, to find an explicit solution to Eq. (33) (or its helical modification) and obtain $\{u_\tau^{(j)}, u_v^{(j)}, \omega^{(j)}\}$ as rational functions in ℓ_2 and ℓ_3 for $j = 1$ and $j = 2$, respectively. However, an analytical integration of such functions does not appear to be possible, as the coefficients in these polynomials depend in a nontrivial way on β and θ.

We can, however, make some asymptotic progress by considering $d = D/L$ to be small, an assumption supported by experiments. Indeed according to Shaevitz *et al.* [10], $v_0 = v_k \cos\phi \approx 7.5\ \mu$m/s, $\tau_p \approx 0.25$ s, and $L \approx 6\ \mu$m, hence $d \approx 1/3$. Moreover, as observed *a posteriori* in our simulations in Fig. 9, both the swimming speed and the efficiency depend only weakly on the interkink distance, and therefore the maximum swimming speed and efficiency are achieved at almost the same value of θ, for any value of d.

We therefore consider the asymptotic limit $d \ll 1$ and expand $\mathbf{x}_T$ in powers of d. To leading order, the components of the total displacement are obtained as

$$x_T^{(h)} = [(1-\beta)(1+\cos\theta)\sin\theta + \beta f \sin\theta]d + \mathcal{O}(d^2), \tag{62}$$

$$y_T^{(h)} = [(1-\beta)\sin^2\theta + \beta f(1-\cos\theta)]\frac{d}{\beta} + \mathcal{O}(d^2). \tag{63}$$

Substituting Eq. (32) into Eqs. (62) and (63), with f as given in Eq. (24) and $\beta^h = 1/2$, and further substituting into Eq. (50) gives access to the asymptotic solution for the swimming speed as

$$\left(\frac{v_s^{(h)}}{v_k}\right)^2 = \frac{\sin^4\theta(5-3\cos\theta)^2(85-3\cos\theta+43\cos^2\theta+3\cos^3\theta)}{8(7-\cos\theta)^2(3+\cos\theta)^2}d^2 + \mathcal{O}(d^3). \tag{64}$$

Furthermore, the total dissipated energy is given, at leading order in d, by

$$\hat{W}^{(h)} = \frac{(1+\cos\theta)(17+4\cos\theta+3\cos^2\theta)}{7-\cos\theta}d + \mathcal{O}(d^2). \tag{65}$$

The swimming efficiency is then obtained by substituting Eqs. (64) and (65) into Eq. (57), and we obtain

$$\eta^{(h)} = \frac{\sin^2\theta(5-3\cos\theta)^2(85-3\cos\theta+43\cos^2\theta+3\cos^3\theta)}{2(7-\cos\theta)^2(3+\cos\theta)(17+4\cos\theta+3\cos^2\theta)}d + \mathcal{O}(d^2). \tag{66}$$

We illustrate in Fig. 9 the comparison between the full numerical solutions of our model and the asymptotic expansion up to order d^3, for values of the interkink distance between $d = 0.05$ and $d = 0.25$. Although the agreement is quantitative only for the smallest values of d, both the swimming speed and the efficiency depend only weakly on d and the maxima are achieved at approximately the same value of θ for all d. The bending angle, $\theta_{v_s}^*$, that maximizes the swimming speed (at leading order in d) satisfies $g_{v_s}(\cos\theta_{v_s}^*) = 0$, where

$$g_{v_s}(\xi) = 14\,425 + 24\,343\xi - 19\,895\xi^2 + 25\,631\xi^3 - 15\,229\xi^4 - 4963\xi^5 + 219\xi^6 + 45\xi^7, \tag{67}$$

whose only real root of modulus less than unity is $\xi \simeq -0.391$, which corresponds to optimal values of $\theta_{v_s}^* \simeq 113^\circ$ or $\phi_{v_s}^* \simeq 33.5^\circ$. On the other hand, for the swimming efficiency, the angle θ_η^* that maximizes $\eta^{(h)}$ (at leading order in d) satisfies $g_\eta(\cos\theta_\eta^*) = 0$, where

$$\begin{aligned} g_\eta(\xi) = {} & 115\,175 + 116\,603\xi - 80\,524\xi^2 + 132\,372\xi^3 \\ & - 73\,638\xi^4 - 40\,830\xi^5 - 18\,348\xi^6 - 3372\xi^7 - 9\xi^8 + 27\xi^9, \end{aligned} \tag{68}$$

whose only real root of modulus less than unity is $\xi \simeq -0.539$, which corresponds to an optimum of $\theta_\eta^* \simeq 122^\circ$ or $\phi_\eta^* \simeq 29^\circ$. Our mathematical model predicts therefore optimal shapes for *Spiroplasma* that are close to those seen experimentally ($\phi \simeq 35^\circ$).

VI. DISCUSSION

A. Summary

In this work we have derived a hydrodynamic model to describe the motility of *Spiroplasma*. Our simple model includes details of the helical geometry of the bacterium at a coarse-grained level and is able to capture the main features of *Spiroplasma* swimming motion. Our results confirm those of previous numerical simulations [21,22] which also agree with experimental observations [10,12–18]. In detail, our model predicts that (i) *Spiroplasma* swims in the direction opposite to the kink pair propagation, at a swimming speed v_s proportional to the kink speed v_0; (ii) for values of the dimensionless interkink distance $d = D/L$ in the experimental range, the swimming speed is $v_s \simeq 1$–2 μm/s; (iii) in the case where the motion occurs in a plane, we found that *Spiroplasma*

does not reorient after one complete stroke; and (iv) the maximum swimming efficiency is achieved for a pitch angle of $\phi_\eta^* \simeq 29^\circ$ while the maximum swimming speed is attained at $\phi_{v_s}^* = 33.5^\circ$.

B. Comparison with experiments

Experimental values for the swimming speed range between $v_s \simeq 1$ and $v_s \simeq 3$ μm/s, while the kink speed lies between $v_k \simeq 10$ and $v_k \simeq 40$ μm/s. Similar values are also reported in the numerical study by Wada and Netz [22]. Therefore our theoretical results are consistent with both experiments and previous computational models.

The numerical simulations of our model show that both the swimming speed and the efficiency depend only weakly on the interkink distance, which allowed us to determine the position of their maxima by considering only the lowest-order term in their asymptotic expansions in powers of d. Our model predicts that the maximum swimming speed is attained at a pitch angle $\phi_{v_s}^* = 33.5^\circ$ very close to the experimental measured one, $\phi = 35^\circ$. Although the maximum efficiency is not achieved at the same value of ϕ, the value of the efficiency $\eta(\phi = 35^\circ)$ is not far from the maximum. For the case $d = 0.25$, for instance, $\eta(\phi = 35^\circ) \simeq 0.13$, which differs by 7% with respect to the maximum $\eta_{\max} \simeq 0.14$. Considering the fact that we are modeling the dynamics of the helical domains only at a coarse-grained level, we regard this agreement as excellent, and it is also consistent with previous numerical models [21,22].

C. Motion in three dimensions

In previous numerical simulations, it has been observed that *Spiroplasma* trajectories are almost rectilinear [21,22], a result which is consistent with our theoretical prediction of no reorientation in the case of planar motion. Movement in a plane will take place only if the right-handed domains are parallel; in other words, there is planar motion only if the angle ψ in Sec. II C vanishes. In the case where we have $D = nP$ with $n \in \mathbb{N}$, then the axes of the right-handed domains are parallel. According to experiments $d \simeq 1/3$ (see Sec. IV), which means that $D \simeq 2$ μm. On the other hand, the pitch of the cell body is $P \simeq 1$ μm, hence $D \simeq 2P$. Therefore, the assumption of planar motion is the biologically relevant limit.

Fluctuations in the time between chirality transformations may be accounted for by considering the angle ψ to be nonvanishing but small. In this case we can expand the linear and angular velocities in powers of ψ, $\mathbf{u} = \mathbf{u}_0 + \psi\mathbf{u}_1 + \mathcal{O}(\psi^2)$ and $\boldsymbol{\omega} = \boldsymbol{\omega}_0 + \psi\boldsymbol{\omega}_1 + \mathcal{O}(\psi^2)$, where $(\mathbf{u}_0, \boldsymbol{\omega}_0)$ correspond to the planar motion presented above. By expanding the resistance matrix and the right-hand side of Eq. (18), it is possible to show that $\mathbf{u}_0 \cdot \mathbf{u}_1 = \boldsymbol{\omega}_0 \cdot \boldsymbol{\omega}_1 = 0$. As a consequence, for small enough values of ψ, the motion corresponds to a helix with a large radius, $R_h \sim \psi^{-1}$, and the trajectories are effectively straight.

D. Diffusion

Experimental observations reveal that the kink propagation can be reversed, and in homogeneous media this reversal rate is constant [18]. According to our model, the cell body does not reorient after one stroke. Moreover, by reversibility of Stokes flow, we know that the cell body traces back its path when the chirality transformation is reversed. The consequence is rather severe, as it means that when swimming in free space, the cell body can only reorient by thermal noise.

This motion can be modeled as a run-reverse pattern, characterized by a persistence parameter $\kappa = \langle \cos\theta_t \rangle$ and a mean path length $v_s\lambda_r^{-1}$ [29]. Here θ_t is the angle between tumbling events, which for a run-reverse pattern is $\theta_t = \pi$, hence $\kappa = -1$. The swimming speed is v_s and λ_r^{-1} is the mean arrival time for a reversal event, which we assume follows an exponential distribution. In the absence of thermal noise, the velocity correlation function is given by $\mathcal{C}(t) = v_s^2 e^{-2\lambda_r t}$. Assuming that the process that generates the chirality change is independent of thermal noise, the velocity correlation function including thermal noise is then simply given by $\mathcal{C}(t) = v_s^2 e^{-2(\lambda_r + D_r)t}$, where $D_r = k_B\Theta\zeta_r^{-1}$ is the rotational diffusion coefficient, with k_B the Boltzmann constant and Θ the

absolute temperature. Here we use ζ_r to denote the rotational drag coefficient, given approximately by $\zeta_r \simeq \pi\mu L^3/3\ln(L/R)$, where L and R are the length and radius of *Spiroplasma*, and μ is the dynamic viscosity of the medium [30]. Integrating $\mathcal{C}(t)$ twice and taking the long-time limit, we obtain the effective diffusion constant $4D_e = 3D_\perp + v_s^2/(2D_r + 2\lambda_r)$, where $D_\perp = k_B\Theta\zeta_\perp^{-1}$ is the translational thermal diffusion coefficient. Note that the translational drag $\zeta_\perp$ is given by Eq. (30) with $\zeta_\perp^h = 4\pi\mu L/\ln(L/R)$ [30]. This result is consistent with the analysis presented by Wada and Netz [21] and extends it to include persistence that, for a run-reverse motion, hinders diffusion.

E. Chemotaxis

It is also known that *Spiroplasma* cells can perform chemotaxis. Although it is not yet fully understood, it has been observed that the presence of certain amino acids changes the reversal rate of kink propagation, and the cell appears to twitch [18,23,24]. When viewed as a run-reverse motion with rotational diffusion, a change in the reversal rate modifies the mean path length. Indeed a lower reversal rate in regions of high attractant concentration results in longer trajectories before a change in the direction of motion occurs, and as a result, the random walk is biased up the gradient. Experimental observations have shown that the biochemical machinery that controls chemotaxis in *Spiroplasma* is unrelated to the conventional two-component system of other bacteria such as *E. coli* [18]. Nevertheless, given the small size of *Spiroplasma*, we can still assume that, similarly to *E. coli*, *Spiroplasma* can only measure differences in chemical concentrations over time. Under this assumption, the de Gennes model for chemotaxis can be applied [31]. In this approximation, the drift speed of the cell is given by $v_d = v_s^2|\nabla c|\lambda_k G(K)/(2\lambda_k + 2D_r)^2$, where the function G is given by $G(K) = \int e^{-2(\lambda_k+D_r)t}K(t)\,\mathrm{d}t$ and $K(t)$ is the cell memory kernel satisfying the adaptability condition $\int_0^\infty K\,\mathrm{d}t = 0$. The experimental observations by Liu *et al.* [18] suggest that *Spiroplasma eriocheiris* performs chemotaxis without adaptation. On the other hand, Daniels and Longland [24] observed that *Spiroplasma melliferum* responds only to gradients and not to absolute values of concentration, which suggest adaptation. In any case, the de Gennes model is appropriate, as we can assume either that the time scale for adaptation is very large but finite or that *Spiroplasma* can sense changes in concentrations instantaneously; the latter was shown to be included in the de Gennes model by Locsei [32].

F. Outlook

Further extensions to our model could consider the presence of nonhomogeneous viscosity fields. It is known that *Spiroplasma*, as other helical-shaped bacteria, swims faster in more viscous environments [23,33,34]. While the swimming speed increases, the kink velocity remains the same. As proposed by Magariyama and Kudo [35], in a linear-polymer solution, the motion of a slender rod is restricted mostly in the perpendicular direction to its axis, as long as its length is much larger than the characteristic size of the polymer network. In that case, we can approximate the new drag ratio by $\beta_p \simeq (\mu_0/\mu_p)\beta$, where μ_p is the viscosity of the polymeric solution and μ_0 that of the standard medium. Assuming that the interkink distance does not depend on the viscosity of the medium and noting that at leading order $|\mathbf{x}_T| \propto (3 + \cos\theta - \beta)$, we should expect higher swimming velocities for increasing viscosity. Besides an increase in swimming speed, it would also be possible for a nonhomogeneous viscosity field to generate a torque that reorients the cell body. Like the bacterium *H. pylori*, living in the mucous layer in the stomach [36], *Spiroplasma* should then be able to display viscotaxis [37].

ACKNOWLEDGMENTS

We thank Boyuan Liu (Ecole Polytechnique) for related work carried out in a summer internship. This project has received funding from the European Research Council (ERC) under the European Union's Horizon 2020 research and innovation program (Grant Agreement No. 682754 to E.L.).

[1] E. M. Purcell, Life at low Reynolds number, Am. J. Phys. **45**, 3 (1977).
[2] G. I. Taylor, Analysis of the swimming of microscopic organisms, Proc. R. Soc. London A **209**, 447 (1951).
[3] G. J. Hancock, The self-propulsion of microscopic organisms through liquids, Proc. R. Soc. London A **217**, 96 (1953).
[4] J. Lighthill, Flagellar hydrodynamics, SIAM Rev. **18**, 161 (1976).
[5] A. T. Chwang and T. Y. Wu, A note on the helical movement of micro-organisms, Proc. R. Soc. London B **178**, 327 (1971).
[6] H. C. Berg, *E. coli in Motion* (Springer, New York, 2004).
[7] J. B. Waterbury, J. M. Willey, D. G. Franks, F. W. Valois, and S. W. Watson, A cyanobacterium capable of swimming motility, Science **230**, 74 (1985).
[8] K. Ehlers and G. Oster, On the mysterious propulsion of *Synechococcus*, PLoS ONE **7**, e36081 (2012).
[9] R. F. Whitcomb, The genus *Spiroplasma*, Annu. Rev. Microbiol. **34**, 677 (1980).
[10] J. W. Shaevitz, J. Y. Lee, and D. A. Fletcher, *Spiroplasma* swim by a processive change in body helicity, Cell **122**, 941 (2005).
[11] N. W. Charon and S. F. Goldstein, Genetics of motility and chemotaxis of a fascinating group of bacteria: The spirochetes, Annu. Rev. Genet. **36**, 47 (2002).
[12] S. Trachtenberg and R. Gilad, A bacterial linear motor: Cellular and molecular organization of the contractile cytoskeleton of the helical bacterium *Spiroplasma melliferum* BC3, Mol. Microbiol. **41**, 827 (2002).
[13] R. Gilad, A. Porat, and S. Trachtenberg, Motility modes of *Spiroplasma melliferum* BC3: A helical, wall-less bacterium driven by a linear motor, Mol. Microbiol. **47**, 657 (2003).
[14] S. Trachtenberg, R. Gilad, and N. Geffen, The bacterial linear motor of *Spiroplasma melliferum* BC3: From single molecules to swimming cells, Mol. Microbiol. **47**, 671 (2003).
[15] S. Trachtenberg, S. B. Andrews, and R. D. Leapman, Mass distribution and spatial organization of the linear bacterial motor of *Spiroplasma citri* R8A2, J. Bacteriol. **185**, 1987 (2003).
[16] S. Trachtenberg, The cytoskeleton of *Spiroplasma*: A complex linear motor, J. Mol. Microb. Biotech. **11**, 265 (2006).
[17] S. Trachtenberg, Shaping and moving a *Spiroplasma*, J. Mol. Microb. Biotech. **7**, 78 (2004).
[18] P. Liu, H. Zheng, Q. Meng, N. Terahara, W. Gu, S. Wang, G. Zhao, D. Nakane, W. Wang, and M. Miyata, Chemotaxis without conventional two-component system, based on cell polarity and aerobic conditions in helicity-switching swimming of *Spiroplasma eriocheiris*, Front. Microbiol. **8**, 58 (2017).
[19] D. Nakane, T. Ito, and T. Nishizaka, Coexistence of two chiral helices produces kink translation in spiroplasma swimming, J. Bacteriol **202**, e00735-19 (2020).
[20] J. Yang, C. W. Wolgemuth, and G. Huber, Kinematics of the Swimming of *Spiroplasma*, Phys. Rev. Lett. **102**, 218102 (2009).
[21] H. Wada and R. R. Netz, Model for Self-Propulsive Helical Filaments: Kink-Pair Propagation, Phys. Rev. Lett. **99**, 108102 (2007).
[22] H. Wada and R. R. Netz, Hydrodynamics of helical-shaped bacterial motility, Phys. Rev. E **80**, 021921 (2009).
[23] M. J. Daniels, J. M. Longland, and J. Gilbart, Aspects of motility and chemotaxis in spiroplasmas, Microbiology **118**, 429 (1980).
[24] M. J. Daniels and J. M. Longland, Chemotactic behavior of spiroplasmas, Curr. Microbiol. **10**, 191 (1984).
[25] R. G. Cox, The motion of long slender bodies in a viscous fluid. Part 1. General theory, J. Fluid. Mech. **44**, 791 (1970).
[26] H. Hotani, Light microscope study of mixed helices in reconstituted *Salmonella* flagella, J. Mol. Biol. **106**, 151 (1976).
[27] R. E. Goldstein, A. Goriely, G. Huber, and C. W. Wolgemuth, Bistable Helices, Phys. Rev. Lett. **84**, 1631 (2000).
[28] See Supplemental Material at http://link.aps.org/supplemental/10.1103/PhysRevFluids.5.093102 for the video shows the *Spiroplasma* swimming gait. Blue and red lines represent the different helical domains, right and left handed respectively. The trajectory of the center of mass is represented by the black line,

the cross indicates the initial position and the circles indicate the position at the end of a stroke. Note that *Spiroplasma* swims in the opposite direction to the kink pair propagation.

[29] P. S. Lovely and F. W. Dahlquist, Statistical measures of bacterial motility and chemotaxis, J. Theor. Biol. **50**, 477 (1975).

[30] M. Doi, *The Theory of Polymer Dynamics (International Series of Monographs on Physics)* (Oxford University Press, New York, 1988).

[31] P.-G. de Gennes, Chemotaxis: The role of internal delays, Eur. Biophys. J. **33**, 691 (2004).

[32] J. T. Locsei, Persistence of direction increases the drift velocity of run and tumble chemotaxis, J. Math. Biol. **55**, 41 (2007).

[33] G. E. Kaiser and R. N. Doetsch, Enhanced translational motion of *Leptospira* in viscous environments, Nature **255**, 656 (1975).

[34] K. Takabe, H. Tahara, Md. S. Islam, S. Affroze, S. Kudo, and S. Nakamura, Viscosity-dependent variations in the cell shape and swimming manner of *Leptospira*, Microbiology **163**, 153 (2017).

[35] Y. Magariyama and S. Kudo, A mathematical explanation of an increase in bacterial swimming speed with viscosity in linear-polymer solutions, Biophys. J. **83**, 733 (2002).

[36] S. A. Mirbagheri and H. C. Fu, *Helicobacter Pylori* Couples Motility and Diffusion to Actively Create a Heterogeneous Complex Medium in Gastric Mucus, Phys. Rev. Lett. **116**, 198101 (2016).

[37] B. Liebchen, P. Monderkamp, B. ten Hagen, and H. Löwen, Viscotaxis: Microswimmer Navigation in Viscosity Gradients, Phys. Rev. Lett. **120**, 208002 (2018).